

Evolution of laser microfilaments in the wake of a femtosecond driving pulseD. A. Romanov^{1,2,*} and R. J. Levis^{1,3}¹*Center for Advanced Photonics Research, College of Science and Technology, Temple University, Philadelphia, Pennsylvania 19122, USA*²*Department of Physics, Temple University, Philadelphia, Pennsylvania 19122, USA*³*Department of Chemistry, Temple University, Philadelphia, Pennsylvania 19122, USA*

(Received 12 March 2013; published 12 June 2013)

A theoretical model for subnanosecond evolution of a nonequilibrium, inhomogeneous free-electron gas in a laser filament or microfilament wake channel is presented. The spatial distributions of electron density and temperature calculated in axially symmetric geometry as a function of time reveal dynamics on the picosecond time scale that is principally driven by a combination of thermal conduction in the electron gas and impact ionization of residual neutral atoms. At high laser intensity, the electron density evolves into a widened distribution with a sharp edge while the temperature distribution evolves to a central peak surrounded by a wide plateau. At low laser intensity, little change is seen in the electron density while the temperature again evolves to a wide plateau. The calculations show that the homogeneous electron-density approximation becomes progressively invalid at higher laser intensity. Pump-probe experiments addressing Fraunhofer diffraction patterns, four-wave mixing, and dynamic Rabi sidebands are proposed for experimental verification of the results.

DOI: [10.1103/PhysRevA.87.063410](https://doi.org/10.1103/PhysRevA.87.063410)

PACS number(s): 32.80.Rm, 42.65.Jx, 52.38.Hb

I. INTRODUCTION

Laser filamentation in atmospheric-pressure gases has become an area of intense investigation [1–3] due to both the unique, coupled light-matter structure created in the filament [4–6] and the novel physical and chemical processes the filament enables in its wake channel [7–9]. The position of filamentation along the laser beam path can be controlled using negative chirp of the laser pulses, which delays the self-focusing collapse [10]. More complicated, adaptive modes of control have been also demonstrated that include both the location and extent of the filament [11]. Moreover, filamentation was shown to result in spatial, temporal, and spectral structures of considerable complexity [12,13]. The outcomes of these control efforts are transferred to the local physical state of the medium that continues evolving long after the strong laser field subsides, including electronic and nuclear modes of motion [14,15]. Here we consider the formation of a filament wake channel whose main distinct characteristic is the presence of hot free-electron gas.

Strong-field ionization of the medium is an integral part of the filamentation process, preventing the ultimate collapse of the beam [1,3]. The emerging free-electron gas provides a negative contribution to the refractive index that balances the Kerr self-focusing. (Despite recent challenges related to the controversial role of higher-order Kerr effect [16,17] the plasma paradigm has been successfully maintained [18–21].)

Once generated in the filament, the free-electron gas left in the wake of the laser pulse is open to various pump-probe experiments and practical applications [9,22–24]. Typically, the free-electron density achieved is rather low, because the ionization rate is stabilized upon reaching the balance with the Kerr focusing, so that only about 0.1% of the gas molecules present in the filament become ionized. A second nanosecond-duration laser pulse has been used to increase the electron concentration in the filament wake channel and

to make this concentration amenable to control through an avalanche mechanism [25]. This so-called igniter-heater scheme has been recently demonstrated in a proof-of-concept experiment [26], in which dense electron-gas channels of up to 10 cm in length were generated in air through the joint application of copropagating 500-fs, 15-mJ igniter and 10-ns, 3-J heater pulses. The second approach to obtaining controllable, high-electron-density wake channels is to use prefocused laser beams. Tight focusing has been shown [23,24,27,28] to produce so-called microfilaments of ~ 30 nm in diameter and < 1 cm in length, with free-electron density reaching 10^{18} – 10^{19} cm⁻³.

Various experimental approaches have been used to investigate the free-electron density n in filaments and microfilaments and its transient evolution. Longitudinal diffraction of a probe beam was successfully utilized to investigate the dependence of n on the focusing conditions [27] and dynamics on the subnanosecond time scale [29]. Recently, Rayleigh microwave scattering [30] was used for studies of temporal evolution of n . Wave-front interferometry [31,32] has been employed for spatial or temporal characterization of n in filaments [33] with picosecond time resolution. In the case of microfilaments, the entangled transient dynamics of n and the electron temperature T has been also traced indirectly in a number of pump-probe experiments, including four-wave mixing in boxCARS geometry [23] and dynamic Rabi sidebands [24].

Some aspects of electron-gas evolution in the femtosecond pulse wake have been explored theoretically [23,34,35]. In particular, in a model system of hydrogen atoms, the anisotropic initial distribution of free electrons resulting from strong-field ionization was obtained and then subjected to quantum Monte Carlo analysis of the many-body electron dynamics. This analysis revealed two distinct relaxation steps, concurrent with earlier experimental observations [36]. First, the electron momentum distribution relaxes towards a hot nonequilibrium isotropic distribution. This first step is followed by a slower relaxation towards a quasiequilibrium configuration that is reached on a picosecond time scale [34]. In our analysis of nonlinear optical properties of microfilament wake channels

*Corresponding author: daroman@temple.edu

in a series of noble gases, we concentrated on a later stage of the electron system evolution as probed via four-wave mixing in the boxCARS geometry [23,35]. The dependence of the four-wave-mixing signal on a subnanosecond-time-scale delay of the probe after the excitation pulse is mainly determined by two processes: (i) the rise of free-electron concentration due to impact ionization; and (ii) the increase in ponderomotive grating contrast due to electron cooling. Thus, the atom-specific dynamics of the four-wave-mixing response carries information of the underlying transient dynamics of this highly nonequilibrium system. However, in the four-wave-mixing signal the information regarding free-electron concentration is inseparably entangled with the information regarding the effective electron temperature. In some cases (notably, in argon gas) another, independent source of entangled information on the free-electron-density and temperature dynamics can be provided by the phenomenon of dynamic Rabi sidebands related to the manifold of excited states [24]. The contrast of spectral interference patterns in the sidebands depends on the decoherence rate that is mainly determined by the ambient hot electron gas [37].

All theoretical investigations to date have been carried out for spatially homogeneous electron distributions. The initial distributions of the free-electron density and temperature after the ionizing strong-field laser pulse, however, are decidedly inhomogeneous, with the transverse length scale that can be as small as ~ 10 nm. This inhomogeneity may drastically modify relaxation processes as the relaxation in the surface region may differ considerably from its bulk counterpart. The purpose of this paper is to investigate the role of such inhomogeneities on the subnanosecond transient processes in a filament or microfilament wake channel and to outline possible implications regarding nonlinear optical characteristics of the channels.

II. THE SCENARIO

Once the gaseous medium becomes partially ionized by the strong laser field, $E = E_0(t) \cos[\omega t + \varphi(t)]$, the dynamics of free electrons is dominated by two processes. First, as the electrons emerge in the continuum, they immediately accelerate to higher kinetic energies by ponderomotive action of the strong laser field, $U_p = (e^2/4m\omega^2)E_0^2$. In the case of an individual electron in a free space, this ponderomotive energy would decline to zero as the laser intensity subsides and $E_0 \rightarrow 0$ [38]. However, in the relatively dense medium under consideration, these laser-field-driven electrons can scatter elastically from the ions and inelastically from one another. This intensive scattering, which continues throughout and after the laser pulse, effectively thermalizes the electron distribution and establishes the local electron temperature on a subpicosecond time scale [34]. The ensuing slower (on a subnanosecond time scale) evolution of the nonequilibrium and inhomogeneous system created by the femtosecond excitation pulse is driven by the redistribution and spread of this excess energy.

We consider the situation when the energy loss by the hot electron system is mainly due to impact ionization of the remaining neutral atoms. Thus, we neglect the possibility of multiple ionization of a given atom, as well as impact excitation of atoms and ions to higher-lying bound electronic states. The

rate of impact ionization is proportional to the local density of the free electrons and to the local density of available neutral atoms. As an energetic electron is more likely to ionize a neutral atom on impact, this rate should increase with the electron temperature. These dependencies determine relative roles of the center and surface areas of the channel in the ensuing dynamics of the nonequilibrium system. In the center of the channel, there are many free and hot electrons but fewer available neutral atoms. In contrast, in the surface area of the channel, there is a surfeit of available neutral atoms but rather few free electrons, and the temperature of these electrons is initially not high enough to effectively ionize an atom. Thus, one can expect competition between the center and the peripheral regions in the process of free-electron generation, and the balance will depend on the thermal conductivity of the electron gas, that is, the effectiveness of the central electrons to pass their excess energy to the peripheral ones.

III. THE MODEL

The local state of the system is determined by the free-electron density, n , and electron temperature, T , as well as the ion density, n_i , and the density of neutral atoms, n_0 . At the subnanosecond time scale of interest here, we can neglect the changes in the motion of ions and neutral atoms and, accordingly, the changes in the temperature of these heavy particles. Thus, the local value of the ion density $n_i(\mathbf{r}, t)$ is solely determined by the process of generation,

$$\frac{\partial n_i}{\partial t} = G(n, T), \quad (1)$$

which in the case of simple impact ionization is characterized by the generation rate $G(n, T) = \gamma(t)n(n_0 - n_i)$. In contrast to this, the electron density can be redistributed as driven by the electron-gas pressure gradient and the electric forces. The evolution of the electron density is then described by the continuity-generation equation,

$$\frac{\partial n}{\partial t} + \nabla(\mathbf{n}\mathbf{u}) = G(n, T). \quad (2)$$

Then, the ensemble-average electron velocity \mathbf{u} is subject to the momentum equation, which is modified from the standard form [39] to include the generation process:

$$n \left[\frac{\partial \mathbf{u}}{\partial t} + (\mathbf{u}\nabla)\mathbf{u} \right] = -\frac{1}{m} \nabla(nT) + \frac{e}{m} \mathbf{E}n - \mathbf{u}G(n, T) - \nu n\mathbf{u}. \quad (3)$$

Here, in the right-hand side, the first term is actually the pressure gradient; the second, the volume force; the third term stems from the fact that the particles are generated with zero velocity; and the last term signifies the friction of the electron gas against ions and neutral atoms, $\nu(n_0, n_i, T)$ being the phenomenological total elastic collision rate with ions and neutrals (note that we neglect internal viscous forces). The electric field \mathbf{E} in Eq. (3), in turn, is determined by the possible local imbalance of the electron and ion densities through the Poisson equation,

$$(\nabla\mathbf{E}) = 4\pi e (n - n_i). \quad (4)$$

Finally, the electron temperature satisfies the energy balance equation,

$$\begin{aligned} n \left[\frac{\partial}{\partial t} + (\mathbf{u} \cdot \nabla) \right] \left(\frac{3}{2} T \right) + n T (\nabla \mathbf{u}) - \frac{3}{2m} \nabla \left(\frac{n T}{v} \nabla T \right) \\ = -G(n, T) \left(I_p + \frac{3}{2} T - \frac{m u^2}{2} \right) - v n \frac{m u^2}{2}, \end{aligned} \quad (5)$$

where I_p is the ionization potential, and we used the phenomenological relation for the thermal conductivity coefficient, $\kappa = (3nT)/(2mv)$. In what follows, we will neglect terms that are quadratic in u , based on the fact that $(mu^2/2) \ll T$.

As seen in Eqs. (2)–(5), the cooling and spreading electron-gas behavior is essentially determined by the two material coefficients: the generation rate coefficient, $\gamma(t)$, and the collision rate $v(n_0, n_i, T)$. The generation (impact ionization) rate coefficient is given by the ensemble average of the product of energy-dependent total impact ionization cross section, $\sigma(E)$, and the electron thermal velocity: $\gamma(t) = \langle \sigma(E)v \rangle$. Assuming Maxwellian distribution for the thermalized electrons, the ionization rate coefficient as a function of the electron temperature is expressed as

$$\gamma(t) = 2 \sqrt{\frac{2\pi}{mT^3}} \int_{I_p}^{\infty} dE E \sigma(E) \exp\left(-\frac{E}{T}\right). \quad (6)$$

As seen from Eq. (6), at moderate electron temperatures ~ 1 eV, the high-energy tail of the electron distribution is responsible for creating additional ions from neutrals, because only sufficiently energetic free electrons (with the kinetic energy $E > I_p$) are capable of ionizing bound electrons in the remaining neutral atoms. When these energetic electrons collide with atoms to create ions, the high-energy tail tends to be depleted, only to be replenished by the ascendance of lower-energy electrons via thermal equilibration. The result of this process is the increase of local electron concentration and decrease of electron temperature.

Regarding the energy dependence of the ionization cross section $\sigma(E)$, the two limiting cases have been well studied, $E - I_p \ll I_p$ and $E - I_p \gg I_p$. The intermediate range of energies, $E - I_p \sim I_p$, which is of our primary concern, is less popular, so that it is still under discussion which semiempirical expression for $\sigma(E)$ would be the best in this case. However, there is the general agreement [40] that the cross section scales with the ionization potential and the number of electrons in the upper shell, N , as

$$\sigma(E) = N \left(\frac{E_{Ry}}{I_p} \right)^2 \pi a_B^2 \tilde{\sigma}(u), \quad (7)$$

where a_B is the Bohr radius, E_{Ry} is the Rydberg energy, and $\tilde{\sigma}(u)$ is a dimensionless function of the dimensionless argument, $u = (E/I_p) - 1$. For this latter function, we use a simple semiempirical approximation known as the Lotz formula [41],

$$\tilde{\sigma}(u) = \eta \frac{\ln(u+1)}{u+1}, \quad (8)$$

where η is a fitting parameter. This approximation results in the functional dependence,

$$\gamma(T) = -\frac{E_{Ry}}{\hbar} (2\pi)^{3/2} \eta N a_B^3 \left(\frac{E_{Ry}}{I_p} \right)^{3/2} \left(\frac{I_p}{T} \right)^{1/2} \text{Ei} \left(-\frac{I_p}{T} \right), \quad (9)$$

where $\text{Ei}(z)$ is the integral exponential function [42].

The total rate of elastic relaxation in Eqs. (3) and (5) is comprised of the effects of short-range scattering on neutral atoms and the long-range scattering on the Coulomb potential of the ions. The scattering rate of electrons on neutral atoms $v_{\text{neut}} = \pi a_0^2 (n_0 - n_i) \sqrt{T/m}$, where a_0 is a characteristic scattering length on the order of the atomic radius. The scattering rate on the long-range potential of ions is $v_{\text{ion}} = n_i (e^2/T)^2 \sqrt{T/m} \ln(N_D)$, where N_D is the number of electrons in the Debye sphere [43]. The combination of the two processes leads to the total scattering rate of

$$\begin{aligned} v(n_0, n_i, T) = \sqrt{\frac{T}{m}} \left\{ \pi a_0^2 (n_0 - n_i) + \left(\frac{e^2}{T} \right)^2 \right. \\ \left. \times n_i \ln \left[\frac{1}{3e^3} \left(\frac{T^3}{4\pi n} \right)^{1/2} \right] \right\}. \end{aligned} \quad (10)$$

Given expressions (9) and (10), it is convenient in Eqs. (1)–(5) to scale the temperature with the ionization potential, $T = I_p \tilde{T}$; to scale the ion and electron densities with the initial density of neutral atoms, $n_i = \tilde{n}_i n_0$; $n = \tilde{n} n_0$; and to scale time with the impact ionization rate, $t = t_0 \tilde{t}$ where $t_0 = [(E_{Ry}/\hbar)\eta N n_0 a_B^3 (2\pi E_{Ry}/I_p)^{3/2}]^{-1}$. Then, the velocity is scaled as $u = \tilde{u} \sqrt{I_p/m}$ and the scale of spatial variables will be $r_0 = (\sqrt{I_p/m}) / [(E_{Ry}/\hbar)\eta N n_0 a_B^3 (2\pi E_{Ry}/I_p)^{3/2}]$. In the cylindrical coordinate system, the system of equations in dimensionless form is obtained as

$$\frac{\partial \tilde{n}_i}{\partial \tilde{t}} = \tilde{\gamma} \tilde{n} (1 - \tilde{n}_i), \quad (11)$$

$$\frac{\partial \tilde{n}}{\partial \tilde{t}} + \frac{1}{\tilde{r}} \frac{\partial}{\partial \tilde{r}} (\tilde{r} \tilde{n} \tilde{u}) = \tilde{\gamma} \tilde{n} (1 - \tilde{n}_i), \quad (12)$$

$$\frac{\partial \tilde{u}}{\partial \tilde{t}} = -\frac{1}{\tilde{n}} \frac{\partial}{\partial \tilde{r}} (\tilde{n} \tilde{T}) + \tilde{E} - \tilde{u} [\tilde{\gamma} (1 - \tilde{n}_i) + \tilde{v}], \quad (13)$$

$$\begin{aligned} \frac{\partial \tilde{T}}{\partial \tilde{t}} + \tilde{u} \frac{\partial \tilde{T}}{\partial \tilde{r}} + \frac{2}{3} \frac{\tilde{T}}{\tilde{r}} \frac{\partial}{\partial \tilde{r}} (\tilde{r} \tilde{u}) \\ = \frac{1}{\tilde{n} \tilde{r}} \frac{\partial}{\partial \tilde{r}} \left(\tilde{r} \frac{\tilde{n} \tilde{T}}{\tilde{v}} \frac{\partial \tilde{T}}{\partial \tilde{r}} \right) - \tilde{\gamma} (1 - \tilde{n}_i) \left(\tilde{T} + \frac{2}{3} \right), \end{aligned} \quad (14)$$

$$\frac{1}{\tilde{r}} \frac{\partial}{\partial \tilde{r}} (\tilde{r} \tilde{E}) = \beta (\tilde{n} - \tilde{n}_i). \quad (15)$$

Here, the dimensionless coefficients are

$$\tilde{\gamma}(\tilde{T}) = \left(\frac{1}{\tilde{T}} \right)^{1/2} \text{Ei} \left(-\frac{1}{\tilde{T}} \right),$$

$$\begin{aligned} \tilde{v}(\tilde{n}, \tilde{n}_i, \tilde{T}) = \frac{\alpha^2}{(8\pi)^{1/2} \gamma N} \sqrt{\tilde{T}} \left[1 - \tilde{n}_i + \frac{\tilde{n}_i}{\tilde{T}^2} \frac{1}{2\pi \alpha^2} \right. \\ \left. \times \ln \left(\frac{\alpha^3}{36\pi} \frac{1}{n_0 a_0^3} \frac{\tilde{T}^3}{\tilde{n}} \right) \right], \end{aligned} \quad (16)$$

with the system-specific parameters, $\alpha = (I_p a_0)/(E_{Ry} a_B) \sim 1$ and $\beta = \alpha^3/(n_0 a_0^3 \gamma^2 N^2)$. In an atmospheric-pressure gas,

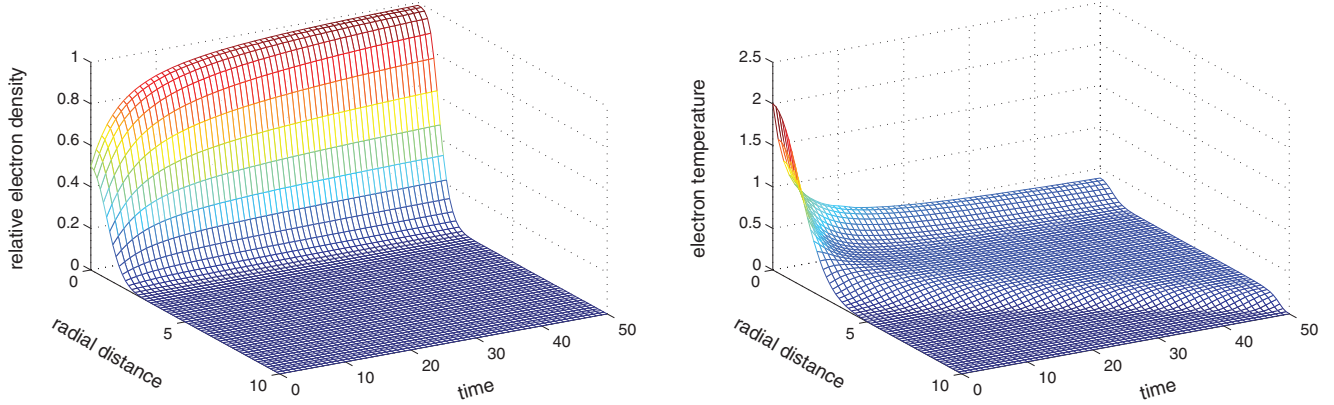


FIG. 1. (Color online) A typical pattern of the correlated evolution of the free-electron-density distribution (left panel) and the electron temperature distribution (right panel) in the microfilament wake channel. The electron density is scaled with the initial density of neutral atoms, n_0 , and the temperature is scaled with the ionization potential, I_p . The time and radial distance are measured in dimensionless units, with the scale factors t_0 and r_0 introduced in the paragraph immediately preceding Eq. (11). In the case of atmospheric-pressure argon gas, $n_0 \approx 2.4 \times 10^{19} \text{ cm}^{-3}$, $I_p \approx 15.76 \text{ eV}$, $t_0 \approx 20 \text{ ps}$, and $r_0 \approx 32 \text{ } \mu\text{m}$.

$n_0 \sim 10^{19} \text{ cm}^{-3}$ and $a_0 \sim 10^{-8} \text{ cm}$, so that $n_0 a_0^3 \ll 1$. The fact that the parameter $\beta \gg 1$ allows us to approximately exclude \tilde{u} , \tilde{E} , and $\tilde{n} - \tilde{n}_i$, and to reduce the system (11)–(15) to the following two approximate equations:

$$\frac{dn_i}{dt} = \tilde{\gamma} n_i (1 - n_i) + \frac{\tilde{\gamma}}{\beta} \frac{1 - n_i}{r} \frac{\partial}{\partial r} \left[\frac{r}{n_i} \frac{\partial}{\partial r} (n_i T) \right], \quad (17)$$

and

$$\begin{aligned} \frac{\partial T}{\partial t} = & \frac{1}{n_i r} \frac{\partial}{\partial r} \left(r \frac{n_i T}{\tilde{v}} \frac{\partial T}{\partial r} \right) - \tilde{\gamma} (1 - n_i) \left(T + \frac{2}{3} \right) \\ & + \frac{T}{\beta} \left(\frac{1}{\tilde{v}} \frac{\partial T}{\partial r} \frac{\partial}{\partial r} \left\{ \frac{1}{r n_i} \frac{\partial}{\partial r} \left[\frac{r}{n_i} \frac{\partial}{\partial r} (n_i T) \right] \right\} \right) \\ & + \frac{1}{n_i} \left(\frac{1}{T} \frac{\partial T}{\partial r} + \frac{2}{3r} \right) \frac{\partial}{\partial t} \left[\frac{1}{n_i} \frac{\partial}{\partial r} (n_i T) \right] \\ & + \frac{2}{3} \frac{\partial}{\partial r} \left\{ \frac{1}{n_i} \frac{\partial}{\partial t} \left[\frac{1}{n_i} \frac{\partial}{\partial r} (n_i T) \right] \right\}. \end{aligned} \quad (18)$$

The second term in the right-hand side of Eq. (17) and everything following $(T + \frac{2}{3})$ in Eq. (18) are small corrections that can be dealt with in the manner of successive iterations. The small difference between the local ion concentration and the free-electron concentration is then found as

$$n - n_i = \frac{1}{\beta r} \frac{\partial}{\partial r} \left[\frac{r}{n_i} \frac{\partial}{\partial r} (n_i T) \right]. \quad (19)$$

When $1/\beta$ -perturbation terms are omitted, the system of equations (17) and (18) presents a complicated form of diffusion-reaction equations. One-component—the one-dimensional version, the so-called Fisher equation [44]—is known to produce solitonlike propagating solutions. Accordingly, we expect the expanding wake channel to have a rather sharp edge favorable for diffraction measurements [28].

IV. RESULTS AND DISCUSSION

The results of the numerical solution of the system of equations (17) and (18) in a typical situation of a microfilament

wake channel are shown in Fig. 1. The dimensionless time and radial distance variables are defined in the preceding section. Referring to a Gaussian transverse profile of the laser beam, we assumed the initial radial distributions of the electron density and temperature to be Gaussian with amplitudes $\tilde{n}_0 = 0.5$ and $\tilde{T}_0 = 2$, and with the small offset in the temperature distribution to account for the ambient room temperature. As anticipated, the diffusion processes have the most effect on the temperature distribution. They lead both to a fast drop of the temperature below two units in radial distance and to the formation of an elevated-temperature radial wave for distances above two units that propagates outward as time increases.

A comparison of the initial Gaussian distributions with those observed at the final step of the simulation time interval is shown in Figs. 2 and 3 for two characteristic cases. Figure 2 corresponds to a high-intensity driving laser pulse (in excess of 10^{14} W/cm^2) and thus to high degree of initial ionization (~ 0.8), which is usually the case in microfilaments [23]. The non-Gaussian shape of the final density profile evolves toward a step-function shape as the ionization in the center of the wake channel engulfs all of the initially neutral atoms. At the same time, the temperature distribution evolves to a bimodal shape, where the central peak is accompanied by a plateau roughly five times wider than the initial spot size. Physically, this feature may be ascribed to the relative effectiveness of the thermoconductivity energy transfer process in comparison with the impact ionization energy transfer process at small values of electron density. The impact ionization rate is proportional to the electron density while the scattering rate also has an electron-density-independent component due to the scattering from neutral atoms [cf. Eqs. (11) and (14)].

The calculation shown in Fig. 3 corresponds to a very low initial degree of ionization, $\sim 0.1\%$, which is typical for most laser filamentation experiments where the intensity in the focal volume is about 10^{13} W/cm^2 . In this case, the change of the initial Gaussian density profile is barely visible; however, the temperature distribution has evolved to an almost stepwise shape. Note, however, that the step edge occurs in a region of a vanishingly small electron density.

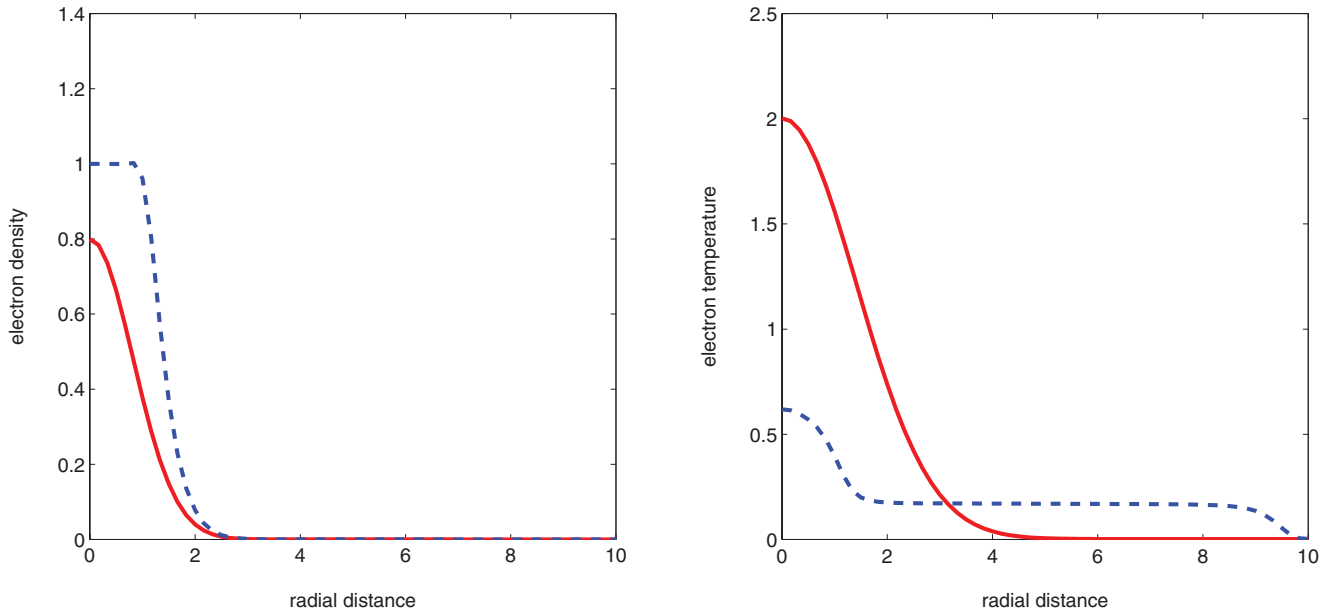


FIG. 2. (Color online) Comparison of the initial and evolved profiles of electron density (left panel) and temperature (right panel) in a microfilament wake channel with considerable initial ionization. Solid (red) lines: initial distributions; dashed (blue) lines: evolved distributions. The electron density is scaled with the initial density of neutral atoms, n_0 , and the temperature is scaled with the ionization potential, I_p . The radial distance is measured in dimensionless units, with the scale factor r_0 introduced in the paragraph immediately preceding Eq. (11). In the case of atmospheric-pressure argon gas, $n_0 \approx 2.4 \times 10^{19} \text{ cm}^{-3}$, $I_p \approx 15.76 \text{ eV}$, and $r_0 \approx 32 \mu\text{m}$.

We next consider the validity of the homogeneous electron-density approximation at the center of the microfilament channel, as one may argue that most experimental manifestations of measurable optical signal come from this region. The calculations show, however, that the expansion of the density and temperature distributions substantially affects their

values at the center of a filament wake channel, as illustrated in Fig. 4. Here, the evolution of the electron-density and temperature values on the axis of a cylindrical channel are compared with the evolution arising from a homogeneous electron gas that starts with the same initial values. As seen in this figure, the accrued difference between the homogeneous

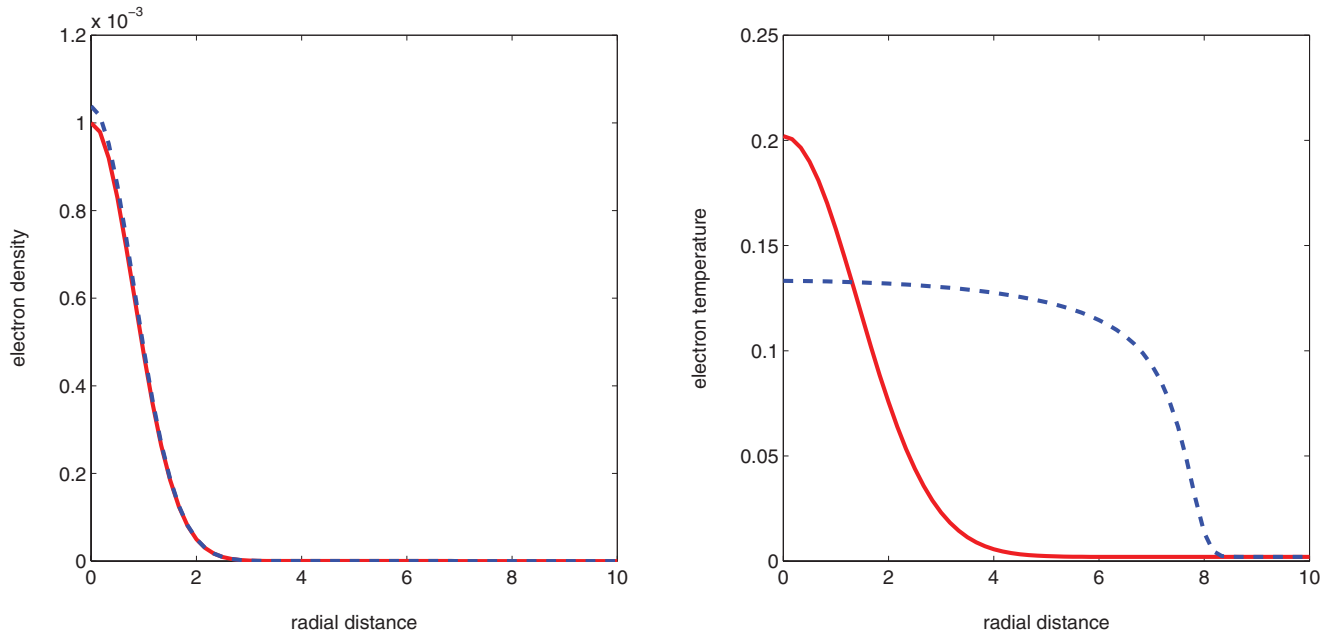


FIG. 3. (Color online) Comparison of the initial and evolved profiles of electron density (left panel) and temperature (right panel) in a filament wake channel with low initial ionization. Solid (red) lines: initial distributions; dashed (blue) lines: evolved distributions. The electron density is scaled with the initial density of neutral atoms, n_0 , and the temperature is scaled with the ionization potential, I_p . The radial distance is measured in dimensionless units, with the scale factor r_0 introduced in the paragraph immediately preceding Eq. (11). In the case of atmospheric-pressure argon gas, $n_0 \approx 2.4 \times 10^{19} \text{ cm}^{-3}$, $I_p \approx 15.76 \text{ eV}$, and $r_0 \approx 32 \mu\text{m}$.

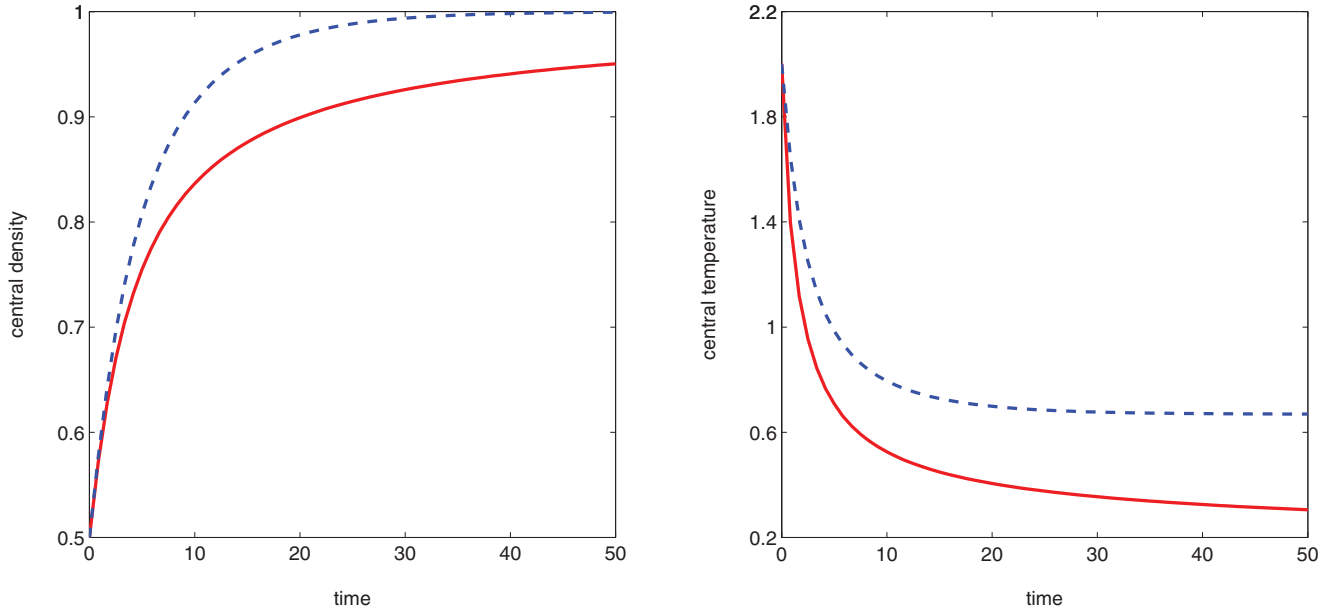


FIG. 4. (Color online) Evolution of the electron density (left panel) and temperature (right panel): solid (red) lines represent the values in the center of a microfilament; dashed (blue) lines, the same in the homogeneous case. The electron density is scaled with the initial density of neutral atoms, n_0 , and the temperature is scaled with the ionization potential, I_p . The time is measured in dimensionless units, with the scale factor t_0 introduced in the paragraph immediately preceding Eq. (11). In the case of atmospheric-pressure argon gas, $n_0 \approx 2.4 \times 10^{19} \text{ cm}^{-3}$, $I_p \approx 15.76 \text{ eV}$, and $t_0 \approx 20 \text{ ps}$.

and inhomogeneous cases is considerable. For instance, in the homogeneous approximation, at the dimensionless time variable value of 30, the central electron density is already saturated; that is, all atoms or molecules are ionized, while the dimensionless electron density in a real channel reaches only the value of 0.9. The difference in the central temperature values is even more pronounced: At the same dimensionless time value of 30, the homogeneous approximation gives the dimensionless temperature of 0.75, while the real-channel value is only 0.38, which is almost two times smaller. When combined, these differences in the density and temperature may considerably modify nonlinear optical characteristics of the channel, which are discussed later in this section. In the case of low initial ionization, which was illustrated in Fig. 3, the differences between those values of electron density and temperature at the center obtained in the homogeneous approximation and those values that result from the real-channel calculations are also appreciable, although in this case these differences take a much longer time to accrue.

The evolution of the electron-density and temperature distributions described above can be accessed and verified experimentally using time-delayed linear and nonlinear light scattering from the wake channel. For instance, in the case of argon at atmospheric pressure, estimates [23] give the characteristic scale values of $t_0 \approx 20 \text{ ps}$ and $r_0 \approx 32 \text{ mm}$. Accordingly, the total interval over which the system evolution is traced in Figs. 1–4 is 1 ns. At atmospheric pressure and room temperature, the density of neutral atoms is about $n_0 \sim 10^{19} \text{ cm}^{-3}$. Then, even in the situation of complete ionization, $n \sim n_0$, the characteristic plasma frequency, $\omega_p = (4\pi ne^2/m_e)^{1/2} \sim 2 \times 10^{14} \text{ s}^{-1}$, that is much smaller than the carrier frequency $\sim 2.5 \times 10^{15} \text{ s}^{-1}$ of the 800-nm laser typically used in these experiments. Thus, the wake channel

is transparent for the probe laser beam and the whole of the transverse electron-density distribution function will be reflected in linear and nonlinear scattering patterns.

The expansion of the electron-density distribution shown in the left panels of Figs. 2 and 3 will determine the evolution of Fraunhofer diffraction patterns in pump-probe experiments introduced in Refs. [27–29,45]. The transverse Fraunhofer diffraction approach developed in Refs. [28,45] seems especially promising in the cases of high electron density, where its accuracy can be improved to enable extraction of the electron-density profile rather than the average density value. Systematic pump-probe investigations of microfilament wake channels should reveal the steepening in electron spatial distribution shown in Fig. 2. Alternatively, the expansion of both the density and the temperature distribution functions as shown in both the left and right panels of Figs. 2 and 3 can be probed using the four-wave mixing in boxCARS geometry [23] and the dynamic Rabi sidebands [24]. In the case of four-wave mixing, the intensity of the output signal is proportional to the free-electron density and inversely proportional to the electron temperature, $I \propto (n/T)^2$ (the temperature dependence reflects the increase in ponderomotive grating contrast due to electron cooling). In Refs. [23,35], the transverse size of the probe laser beams was much larger than that of the microfilament-generating beams, thus measuring the n and T distributions averaged across the channel. The use of tightly focused probe beams will allow the interrogation volume to be scanned across the channel. The dynamic Rabi sidebands [24] occur when a moderately intense picosecond probe pulse interacts with the Ar gas in the wake channel. The complicated spatial-spectral pattern of the sideband emission [46] is ultimately determined by the local electron density and temperature. In particular, the spectral fringe contrast [37] is determined by the dephasing

rate, $\gamma \propto nT^{1/6}$, and thus reflects the n and T distributions as shown in Figs. 2–4.

In both the four-wave-mixing signal and Rabi sideband radiation signal the response contribution from the free-electron concentration is inseparably entangled with the response contribution from the effective electron temperature. Thus, neither of these techniques can solely trace the evolution of both the electron-density distribution and the electron temperature distribution. However, the temperature distribution can be disentangled from the density distribution if the results of these two experiments are analyzed in tandem. Alternatively, either of these nonlinear experiments can be used in conjunction with the results of Fraunhofer diffraction to extract the density and temperature evolution.

V. CONCLUSIONS

We present a theoretical model for subnanosecond evolution of highly nonequilibrium, inhomogeneous free-electron gas in a laser filament or microfilament wake channel. The evolution is principally driven by thermal conduction in the electron gas and impact ionization of residual neutral atoms.

The results show the importance of incorporating spatial effects, especially with regard to the electron temperature. The calculated distributions determine the fast evolution of optical and electronic properties of filament wake channels. In particular, the evolving shape of the electron-density distribution should influence Fraunhofer diffraction patterns. The temperature distribution may also influence various decoherence phenomena including the evolution of four-wave-mixing signal and spatial-spectral patterns of giant Rabi sidebands. In the cases of molecular gases, and gas mixtures, the resulting inhomogeneous distributions of electron density and temperature will initiate inhomogeneous chemical processes, starting with dissociative recombination of molecular ions. The model presented can be augmented to incorporate these processes to describe the ensuing chemical kinetics.

ACKNOWLEDGMENTS

We gratefully acknowledge financial support through AFOSR MURI Grant No. FA9550-10-1-0561 and the National Science Foundation Grant No. CHE0957694.

-
- [1] L. Berge, S. Skupin, R. Nuter, J. Kasparian, and J. P. Wolf, *Rep. Prog. Phys.* **70**, 1633 (2007).
- [2] A. Couairon and A. Mysyrowicz, *Phys. Rep.* **441**, 47 (2007).
- [3] S. L. Chin, *Femtosecond Laser Filamentation* (Springer, New York, 2010).
- [4] A. Couairon, J. Biegert, C. P. Hauri, W. Kornelis, F. W. Helbing, U. Keller, and A. Mysyrowicz, *J. Mod. Opt.* **53**, 75 (2006).
- [5] J. H. Odhner, D. A. Romanov, and R. J. Levis, *Phys. Rev. Lett.* **105**, 125001 (2010).
- [6] C. P. Hauri, R. B. Lopez-Martens, C. I. Blaga, K. D. Schultz, J. Cryan, R. Chirila, P. Colosimo, G. Doumy, A. M. March, C. Roedig, E. Sistrunk, J. Tate, J. Wheeler, L. R. DiMauro, and E. P. Power, *Opt. Lett.* **32**, 868 (2007).
- [7] F. Calegari, C. Vozzi, S. De Silvestri, and S. Stagira, *Opt. Lett.* **33**, 2922 (2008).
- [8] S. Tzortzakis, G. Mechain, G. Patalano, Y. B. Andre, B. Prade, M. Franco, A. Mysyrowicz, J. M. Munier, M. Gheudin, G. Beaudin, and P. Encrenaz, *Opt. Lett.* **27**, 1944 (2002).
- [9] P. R. Hemmer, R. B. Miles, P. Polynkin, T. Siebert, A. V. Sokolov, P. Sprangle, and M. O. Scully, *Proc. Natl. Acad. Sci. USA* **108**, 3130 (2011).
- [10] H. Wille, M. Rodriguez, J. Kasparian, D. Mondelain, J. Yu, A. Mysyrowicz, R. Sauerbrey, J. P. Wolf, and L. Woste, *Eur. Phys. J.: Appl. Phys.* **20**, 183 (2002).
- [11] G. Heck, J. Sloss, and R. J. Levis, *Opt. Commun.* **259**, 216 (2006).
- [12] B. Shim, S. E. Schrauth, A. L. Gaeta, M. Klein, and G. Fibich, *Phys. Rev. Lett.* **108**, 043902 (2012).
- [13] T. D. Grow, A. A. Ishaaya, L. T. Vuong, and A. L. Gaeta, *Phys. Rev. Lett.* **99**, 133902 (2007).
- [14] S. Varma, Y. H. Chen, and H. M. Milchberg, *Phys. Rev. Lett.* **101**, 205001 (2008).
- [15] J. H. Odhner, D. A. Romanov, and R. J. Levis, *Phys. Rev. Lett.* **103**, 075005 (2009).
- [16] V. Loriot, E. Hertz, O. Faucher, and B. Lavorel, *Opt. Express* **17**, 13429 (2009).
- [17] C. Bree, A. Demircan, and G. Steinmeyer, *Phys. Rev. Lett.* **106**, 183902 (2011).
- [18] J. K. Wahlstrand, Y. H. Cheng, Y. H. Chen, and H. M. Milchberg, *Phys. Rev. Lett.* **107**, 103901 (2011).
- [19] J. H. Odhner, D. A. Romanov, E. T. McCole, J. K. Wahlstrand, H. M. Milchberg, and R. J. Levis, *Phys. Rev. Lett.* **109**, 065003 (2012).
- [20] P. Polynkin, M. Kolesik, E. M. Wright, and J. V. Moloney, *Phys. Rev. Lett.* **106**, 153902 (2011).
- [21] J. K. Wahlstrand, Y. H. Cheng, and H. M. Milchberg, *Phys. Rev. Lett.* **109**, 113904 (2012).
- [22] J. Papeer, C. Mitchell, J. Penano, Y. Ehrlich, P. Sprangle, and A. Zigler, *Appl. Phys. Lett.* **99**, 141503 (2011).
- [23] A. Filin, R. Compton, D. A. Romanov, and R. J. Levis, *Phys. Rev. Lett.* **102**, 155004 (2009).
- [24] R. Compton, A. Filin, D. A. Romanov, and R. J. Levis, *Phys. Rev. Lett.* **103**, 205001 (2009).
- [25] P. Sprangle, J. Penano, B. Hafizi, D. Gordon, and M. Scully, *Appl. Phys. Lett.* **98**, 211102 (2011).
- [26] P. Polynkin and J. V. Moloney, *Appl. Phys. Lett.* **99**, 151103 (2011).
- [27] F. Theberge, W. W. Liu, P. T. Simard, A. Becker, and S. L. Chin, *Phys. Rev. E* **74**, 036406 (2006).
- [28] G. Rodriguez, A. R. Valenzuela, B. Yellampalle, M. J. Schmitt, and K.-Y. Kim, *J. Opt. Soc. Am. B* **25**, 1988 (2008).
- [29] J. S. Liu, Z. L. Duan, Z. N. Zeng, X. H. Xie, Y. P. Deng, R. X. Li, Z. Z. Xu, and S. L. Chin, *Phys. Rev. E* **72**, 026412 (2005).
- [30] A. Shashurin, M. N. Shneider, A. Dogariu, R. B. Miles, and M. Keidar, *Appl. Phys. Lett.* **96**, 171502 (2010).
- [31] T. R. Clark and H. M. Milchberg, *Phys. Rev. Lett.* **78**, 2373 (1997).

- [32] S. Y. Chen, G. S. Sarkisov, A. Maksimchuk, R. Wagner, and D. Umstadter, *Phys. Rev. Lett.* **80**, 2610 (1998).
- [33] J. K. Wahlstrand, Y. H. Chen, Y. H. Cheng, S. R. Varma, and H. M. Milchberg, *IEEE J. Quantum Electron.* **48**, 760 (2012).
- [34] B. Pasenow, J. V. Moloney, S. W. Koch, S. H. Chen, A. Becker, and A. Jaron-Becker, *Opt. Express* **20**, 2310 (2012).
- [35] D. A. Romanov, R. Compton, A. Filin, and R. J. Levis, *Phys. Rev. A* **81**, 033403 (2010).
- [36] S. Tzortzakis, B. Prade, M. Franco, and A. Mysyrowicz, *Opt. Commun.* **181**, 123 (2000).
- [37] G. Heck, A. Filin, D. A. Romanov, and R. J. Levis, *Phys. Rev. A* **87**, 023419 (2013).
- [38] P. H. Bucksbaum, R. R. Freeman, M. Bashkansky, and T. J. McIlrath, *J. Opt. Soc. Am. B* **4**, 760 (1987).
- [39] J. A. Bittencourt, *Fundamentals of Plasma Physics* (Springer-Verlag, New York, 2004).
- [40] P. L. Bartlett and A. T. Stelbovics, *Phys. Rev. A* **66**, 012707 (2002).
- [41] S. M. Younger and T. D. Mark, in *Electron Impact Ionization*, edited by T. D. Mark and G. H. Dunn (Springer-Verlag, Wien, New York, 1985), p. 24.
- [42] M. Abramowitz and I. Stegun, *Handbook of Mathematical Functions* (National Bureau of Standards, Washington, DC, 1964).
- [43] A. A. Fridman and L. A. Kennedy, *Plasma Physics and Engineering* (Taylor and Francis, New York, 2004).
- [44] P. Grindrod, *The Theory and Applications of Reaction-Diffusion Equations. Patterns and Waves* (Clarendon Press, Oxford, 1996).
- [45] H. Yang, J. Zhang, Y. Li, J. Zhang, Y. Li, Z. Chen, H. Teng, Z. Wei, and Z. Sheng, *Phys. Rev. E* **66**, 016406 (2002).
- [46] G. Heck, R. Compton, A. Filin, M. Plewicki, D. A. Romanov, and R. J. Levis, *Opt. Lett.* **36**, 3224 (2011).